Applied Catalysis B: Environmental 244 (2019) 502–510

Contents lists available at ScienceDirect

Applied Catalysis B: Environmental

journal homepage: www.elsevier.com/locate/apcatb

Charge compensation doping to improve the photocatalytic and photoelectrochemical activities of Ta_3N_5: A theoretical study

Jiajia Wang[a], Yaqing Jiang[a], Aibin Ma[a,*], Jinghua Jiang[a], Jianqing Chen[a], Mingxue Li[b], Jianyong Feng[c], Zhaosheng Li[c,*], Zhigang Zou[c]

[a] College of Mechanics and Materials, Hohai University, Nanjing, 210098, PR China
[b] Department of Physics, China University of Mining and Technology, Xuzhou, 221116, PR China
[c] National Laboratory of Solid State Microstructures, Department of Physics, Ecomaterials and Renewable Energy Research Center (ERERC), College of Engineering and Applied Sciences, Nanjing University, Nanjing, 210093, PR China

ARTICLE INFO

Keywords:
Ta_3N_5
Photocatalytic
Photoelectrochemical
DFT
Elements doping

ABSTRACT

Ta_3N_5 was potentially a high efficient semiconductor in photocatalytic and photoelectrochemical water splitting but its practical performances were unsatisfactory. The oxygen impurity, which substituted N and acted as an electron donor, was one possible source of the poor photocatalytic and photoelectrochemical activities of Ta_3N_5. In this study, 24 elements, which substituted Ta and acted as the electron acceptor, were codoped with the oxygen impurity to achieve charge compensation in Ta_3N_5. Based on the density functional theory calculations, the defect formation energies, electronic structures and carrier mobility were investigated. The results showed that the charge compensation doping method was able to improve the conduction band position of Ta_3N_5, suggesting that this method was effective to enhance water reduction ability and lower onset potential of Ta_3N_5. The Ti, Zr and Hf elements were found to be more effective than other elements because they were able to keep the carrier mobility of Ta_3N_5. Our calculation results agreed well with experiments and provided useful guidance for future investigations of Ta_3N_5.

1. Introduction

Semiconductor-based photocatalytic or photoelectrochemical (PEC) water splitting is one of the most promising solutions to the energy crises, because it can split water into H_2 and O_2 gases under irradiation of solar light [1–4]. To realize the visible light water splitting, an ideal semiconductor should satisfy two fundamental requirements. One is that its conduction band minimum (CBM) and valence band maximum (VBM) straddle the water reduction (H^+/H_2) and oxidization (H_2O/O_2) potentials. The other is that its band gap should be around 2.0 eV for absorbing the visible portion of solar light. Since the pioneer work on TiO_2 [5], great efforts have been devoted to develop more efficient semiconductors [6–9]. Among the semiconductors investigated to date, the tantalum nitride (Ta_3N_5) has attracted a great of interest because of its suitable band gap (~2.1 eV) and band-edge positions (Fig. 1a), matching well with the requirements of an ideal semiconductor in water splitting [10–14].

Unfortunately, the practical photocatalytic and PEC performances of Ta_3N_5 are unsatisfactory. In recent years, great efforts have been made to improve the activities of Ta_3N_5 [15–27]. Recently, Liu et al. obtained a record 12.1 mA/cm^2 photocurrent of the Ta_3N_5 photoanode [28], which was very close to its theoretical maximum photocurrent (12.9 mA/cm^2). However, their obtained solar-to-hydrogen efficiency of Ta_3N_5 was 2.5%, which was much lower than the theoretical maximum efficiency of Ta_3N_5 (15.9%) [29]. The processes of photocatalytic and PEC water splitting are complex and affected by various factors. To our knowledge, one possible cause of the lower activity of Ta_3N_5 comes from the oxygen impurities. Note that the practical Ta_3N_5 naturally consists of considerable amounts of oxygen impurities, which may be the residual O of Ta_2O_5 precursor after nitridation treatment [30,31]. Furthermore, the oxygen impurities, which substitute N atoms (O_N) in Ta_3N_5, are difficult to be completely removed because they are beneficial to the thermodynamic stabilities of Ta_3N_5 [32]. The ionization energy of O_N in Ta_3N_5 is as low as 0.06 eV, suggesting that the O_N impurity is an effective electron donor in Ta_3N_5 [33].

Effects of O_N impurities on the electronic structures of Ta_3N_5 have been extensively studied and can be summarized in Fig. 1b [33,34]. As an electron donor, electrons donated from O_N are uniformly distributed on Ta atoms and further induce cathodic shift of the CBM of Ta_3N_5. Since the CBM position relative to the water reduction (H^+/H_2)

* Corresponding authors.
E-mail addresses: aibin-ma@hhu.edu.cn (A. Ma), zsli@nju.edu.cn (Z. Li).

https://doi.org/10.1016/j.apcatb.2018.11.076
Received 5 October 2018; Received in revised form 15 November 2018; Accepted 26 November 2018
Available online 26 November 2018
0926-3373/

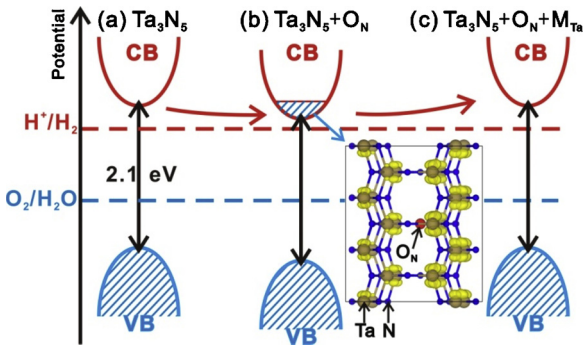

Fig. 1. Schematic diagrams of the band structures of (a) Ta_3N_5, (b) $Ta_3N_5+O_N$ and (c) $Ta_3N_5+O_N+M_{Ta}$. The blue shaded area denotes the electron occupied states. The partial charge density (in yellow) of the CBM of $Ta_3N_5+O_N$ is shown on the right of (b). (For interpretation of the references to colour in this figure legend, the reader is referred to the web version of this article.)

potential reflects the water reduction ability of a semiconductor, the cathodic shift of CBM suggests that O_N impurity is one possible source of the poor water reduction ability of Ta_3N_5. Furthermore, considering that the shift of CBM corresponds to the shift of onset potential for an *n*-type semiconductor, the O_N impurity is also one possible source of the high onset potential of Ta_3N_5 in PEC system [35,36]. Since the O_N impurity is an electron donor, doping an electron acceptor into Ta_3N_5 may be able to eliminate the adverse effects brought by O_N impurity. Then, the electrons donated from O_N, which were originally accepted by Ta atoms, now move to the doped electron acceptor. The charge compensation between electron acceptor and O_N impurity further improves the CBM position of Ta_3N_5 (Fig. 1c). Actually, this charge compensation doping strategy has been realized in recent experiments of Ba-doped [37], Zr-doped [38] and Sc-doped [39] Ta_3N_5. However, besides Ba, Zr and Sc, whether other elements can be doped into Ta_3N_5 to compensate for O_N impurity needs further investigations.

The motivation of this study is to find out more suitable elements that are able to compensate for O_N impurity in Ta_3N_5. We only consider the substitution-type dopant that substitutes Ta atom and form the electron acceptor. Since the valence state of Ta in Ta_3N_5 is +5, elements in eight groups IA, IIA, IIIA, IVA, IB, IIB, IIIB and IVB are theoretically all able to substitute Ta and form the electron acceptor. However, considering that large discrepancy in ionic size is not beneficial to elements substitution, we finally select 24 possible elements which are listed in Table 1. The selection criterion is that the ionic radius of dopant is not larger than twice of that of Ta5+ (0.7 Å).

Density functional theory (DFT) calculation is an effective and popular method in many research fields. DFT calculations are able to calculate various properties such as thermodynamic properties, electronic structures, and reaction pathways, which provide useful insight and guidance for experimental investigations [40–44]. To screen out suitable elements that are able to compensate for O_N impurity from these 24 elements, DFT calculations are performed and three steps will be carried out in this study. Unless explicitly stated, we use symbol 'M' to denote the 24 elements hereinafter. Then, the substitution of M for Ta can be expressed as M_{Ta}. We use '*x*' to express the number of O_N impurities. We firstly calculate defect formation energies of $M_{Ta}+xO_N$ to screen out elements which are thermodynamically more stable in Ta_3N_5. Secondly, based on the elements screened out from the first step, we will calculate electronic structures to screen out elements that are able to improve the CBM position of Ta_3N_5. Thirdly, considering that the carrier mobility plays critical role in photocatalytic and PEC water splitting, carrier effective masses of $M_{Ta}+xO_N$ codoped Ta_3N_5 will be calculated based on the elements screened out from second step.

Table 1
Elements that this study selects to substitute Ta of Ta_3N_5.

Group	Element (ionic radii in Å)	Valence state
IA	Li(0.68)、Na(0.95)、K(1.33)	+1
IIA	Mg(0.65)、Ca(0.99)、Sr(1.13)、Ba(1.35)	+2
IIIA	Al(0.50)、Ga(0.62)、In(0.81)	+3
IVA	Si(0.41)、Ge(0.53)、Sn(0.71)	+4
IB	Cu(0.72)、Ag(1.26)、Au(1.37)	+1
IIB	Zn(0.74)、Cd(0.97)	+2
IIIB	Sc(0.81)、Y(0.93)、La(1.06)	+3
IVB	Ti(0.68)、Zr(0.79)、Hf(0.78)	+4

2. Computational details

2.1. Computational methods and models

The DFT calculations in this study are performed by VASP (5.2) [45,46] with the projected-augmented-wave (PAW [47]) method. The generalized gradient approximation (GGA [48]) in the scheme of Perdew-Burke-Ernzerhof (PBE [49]) is adopted for the exchange-correlation functional. The cutoff energy is 500 eV. Geometry relaxations are performed until the residual forces on each ion converged to be smaller than 0.02 eV $Å^{-1}$. All atomic models are visualized by the VESTA (3.3.1) software [50]. Based on these computational parameters, the relaxed lattice constants of conventional Ta_3N_5 cell are a = 3.91, b = 10.32 and c = 10.35 Å, which agree within the estimated experimental uncertainty (a = 3.89, b = 10.21 and c = 10.26 Å) [51].

In the conventional cell of Ta_3N_5 (Fig. 2a), the Ta atom is coordinated with six neighboring N atoms, while N atoms are coordinated with three or four Ta atoms. To simulate the elements doped Ta_3N_5, a $3\times1\times1$ ($11.73\times10.32\times10.35\ Å^3$) Ta_3N_5 super-cell, which includes 60 N and 36Ta atoms, is built (Fig. 2b). For the $3\times1\times1$ super-cell, the Γ-centered $2\times2\times2$ *k*-point meshes (include 8 *k*-points) is adopted for the Brillouin zone integration. Based on this super-cell, the atomic models of doping $M_{Ta}+O_N$, $M_{Ta}+2O_N$, $M_{Ta}+3O_N$ and $M_{Ta}+4O_N$ into Ta_3N_5 are built and shown in Fig. 2c–f, respectively. The number of O_N (*x*) in $M_{Ta}+xO_N$ depends on the valence state of M_{Ta}. For example, one Li_{Ta} theoretically needs $4O_N$ to keep the charge balance. The positions of O_N impurities in the four doping models are selected based on defect formation energies. More details of the four doping models can be found in SI-1 of the supporting information.

Note that, the GGA-PBE functional is generally sufficient to get reliable thermodynamic and elastic properties. However, due to the underestimation of band gap, the GGA-PBE functional may be not accurate enough to calculate the electronic structures of semiconductors, especially the elements doped and defective semiconductors [52,53]. To make the theoretical simulations close to practical experiments as much as possible, two strategies are employed in this study. One is using the hybrid functional to calculate electronic structures; the other is using chemical potential, which will be introduced in the following section, to calculate defect formation energies. Electronic structures are calculated by the Heyd-Scuseria-Ernzerhof (HSE [54]) hybrid functional. The accuracy of HSE functional is determined by parameters α and ω, which are the fraction of semilocal PBE functional replaced by a screened nonlocal functional and the inverse screening length, respectively. In our calculations, α and ω are set at 25% and 0.2 $Å^{-1}$, respectively, corresponding to the HSE06 functional [55]. Using the HSE06 functional, the calculated band gap of Ta_3N_5 (2.2 eV) is in good agreement with experimental band gap of Ta_3N_5 (about 2.1 eV).

2.2. Defect formation energies calculation method

Defect formation energies in the neutral charge state are defined as [56]:

$$E^f_{defect} = E^t_{defect} - E^t_{bulk} + \sum n_i \Delta\mu_i \quad (1)$$

where E^t_{defect} and E^t_{bulk} are total energies of Ta_3N_5 super-cell with and

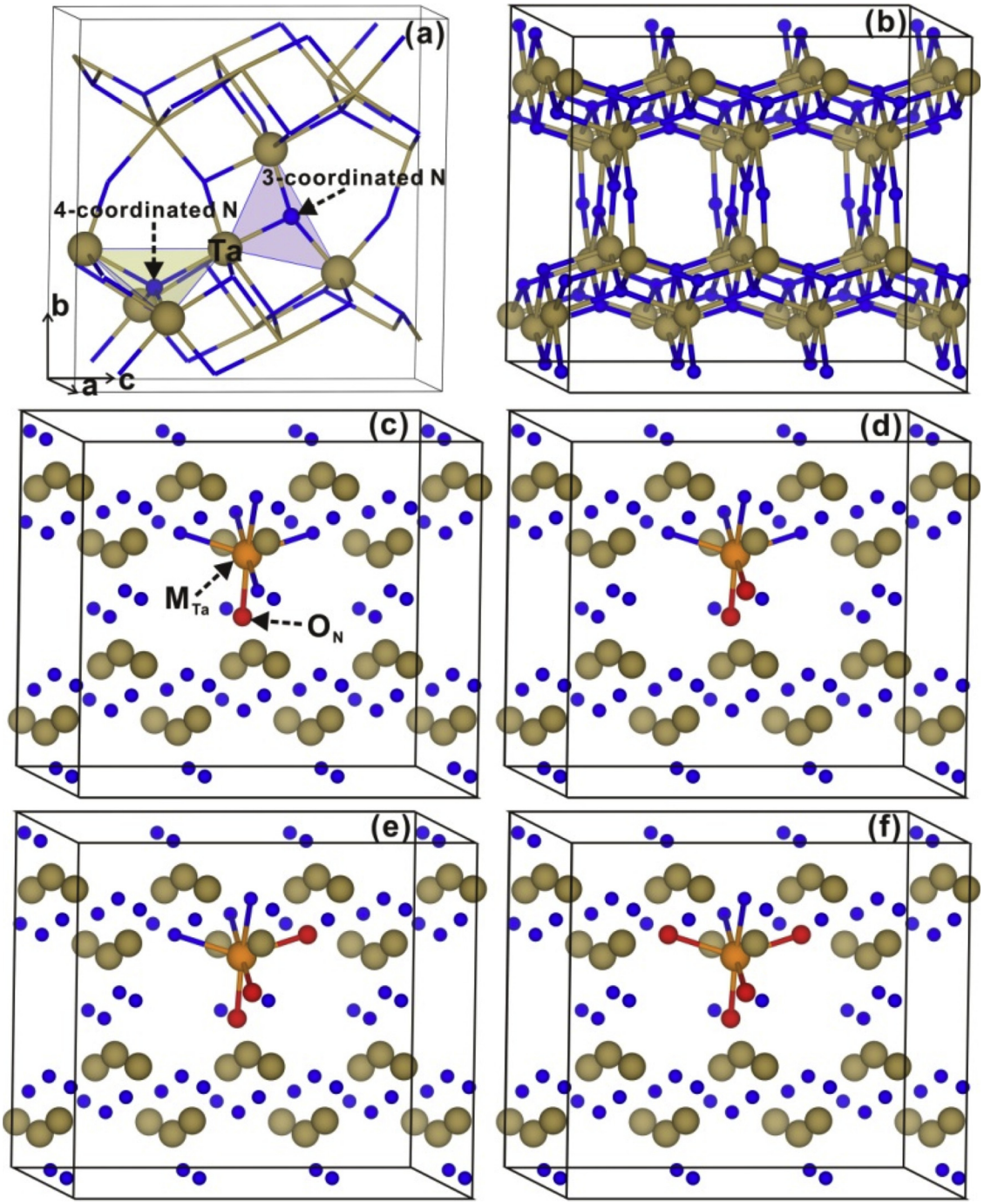

Fig. 2. Atomic structures of the (a) conventional cell and (b) 3 × 1 × 1 super-cell of pure Ta_3N_5. (c)-(f) show atomic structures of $M_{Ta}+O_N$, $M_{Ta}+2O_N$, $M_{Ta}+3O_N$ and $M_{Ta}+4O_N$ codoped Ta_3N_5, respectively.

without defects, respectively, $\Delta\mu_i$ (i=N, O, Ta and M) is the chemical potential of constituent i, and n_i is the number of constituent i. For elements added to and removed from Ta_3N_5, n_i will be in negative and positive value, respectively. For example, formation energy of $Li_{Ta}+4O_N$ codoped Ta_3N_5 can be expressed as:

$$E^f_{defect} = E^t_{defect} - E^t_{bulk} - \Delta\mu_{Li} - 4\Delta\mu_O + \Delta\mu_{Ta} + 4\Delta\mu_N \quad (2)$$

According to the definition of Eq. (1), a more negative formation energy corresponds to an easier elements doping.

As can be seen in the Eq. (1), defect formation energies are dependent on the chemical potentials. In the elements codoped system, chemical potentials must be carefully calculated to ensure the reliabilities of defect formation energies. Using Li-O codoped Ta_3N_5 as an example, Fig. 3 shows chemical potentials of Li and O ($\Delta\mu_{Li}$ and $\Delta\mu_O$) under the N-rich growth condition. Note that, we choose the N-rich growth condition to calculate chemical potentials because of two reasons. First, Ta_3N_5 is prepared by the nitridation treatment of Ta_2O_5 precursor. Second, the N-rich growth condition, which corresponds to the Ta-poor growth condition, is favorable for the M_{Ta} substitution.

To avoid precipitation of possible secondary phases, the values of $\Delta\mu_{Li}$ and $\Delta\mu_O$ can only be selected in the shaded accessible region in Fig. 3. Theoretically, all points in the shaded region can be selected. However, the points at doping limit, where the precipitations are avoided and simultaneously the dopants have larger doping concentrations (smaller formation energies), are generally selected. These

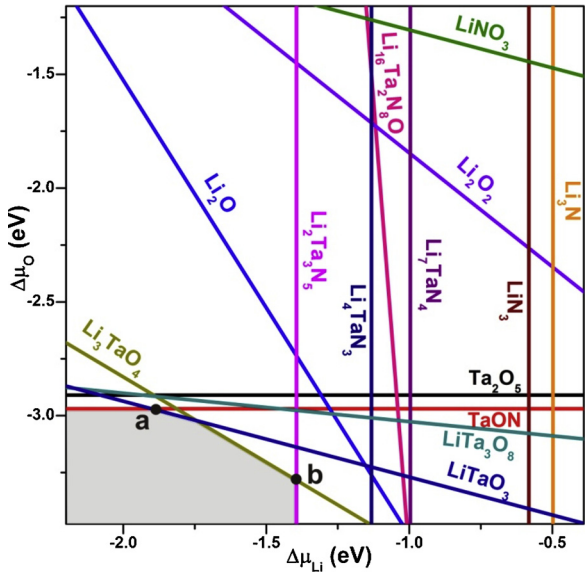

Fig. 3. Chemical potentials of Li and O ($\Delta\mu_{Li}$ and $\Delta\mu_O$) in the Li-O codoped Ta_3N_5 under the N-rich growth condition. The gray shaded region is the accessible range of chemical potentials for equilibrium growth of the Li-O codoped Ta_3N_5. The chemical potentials at points a and b are selected for calculating defect formation energies.

doping limit points are usually at the boundary of the accessible region. For example, the points a and b in Fig. 3 are two doping limit points. In this study, we select the ranges from point a to b, which cover a wide range of chemical potentials. This method of chemical potential selection, which is also adopted in our previous theoretical work [57], is expected to ensure a more reliable and robust analysis of defect formation energies. Chemical potentials of other elements can be found in SI-2 of the supporting information.

3. Results and discussion

3.1. Defect formation energies

In an element doped material, the dopant may locate at the substitutional or interstitial site of the host lattice. To validate whether our considered 24 elements preferentially substitute Ta and coexist with O_N in Ta_3N_5, we firstly calculate defect formation energies in this section. Fig. 4a–x show defect formation energies of doping neutral $M_{Ta}+xO_N$ into Ta_3N_5, where M corresponds to the 24 elements listed in Table 1, as a function of the chemical potential of O ($\Delta\mu_O$). The negative and zero value of $\Delta\mu_O$ correspond to the O-poor and O-rich growth conditions, respectively. In Fig. 4, the formation energies of M_{Ta} and M_{int} (interstitial M) are also calculated and shown in each case. For the convenience of comparison, the defect formation energy results are shown with 8 parts according to the 8 groups of the 24 elements. In each part, defect formation energies use the same vertical axis range.

For each element in six groups IIIA, IVA, IB, IIB, IIIB and IVB (Fig. 4h–x), it is easy to compare thermodynamic stabilities among M_{Ta}, M_{int} and $M_{Ta}+xO_N$ because their discrepancies in formation energies are obvious in the whole chemical potential range. We therefore firstly discuss these six groups: (a) for most dopants, the formation energy of M_{int} is lower than that of M_{Ta}, suggesting the difficulty of doping M_{Ta} into Ta_3N_5. However, our previous work revealed that the charge compensation between Ba_{Ta} and O_N was able to reduce the doping difficulty of Ba_{Ta} [58]. This benefit of charge compensation is clearly reflected in Fig. 4h–x because, for every dopant in Fig. 4h–x, the formation energy of $M_{Ta}+xO_N$ is substantially reduced compared with that of M_{Ta}. In groups IIIA (Fig. 4h–j), IVA (Fig. 4k–m), IIB (Fig. 4q–r), IIIB (Fig. 4s–u) and IVB (Fig. 4v–x), the formation energy of $M_{Ta}+xO_N$ is even lower than that of M_{int} for every dopant. This means that doping $M_{Ta}+xO_N$ into Ta_3N_5 is thermodynamically available for elements in these five groups. (b) In group IB (Fig. 4n–p), although the formation energy of $M_{Ta}+4O_N$ (M = Cu, Ag, Au) is lower than that of M_{Ta}, it is still larger than that of M_{int} for every dopant. This means that the interstitial doping is thermodynamically more stable for Cu, Ag and Au in Ta_3N_5.

Compared with the above six groups, the situations in groups IA and IIA are a little complex: (a) in group IA (Fig. 4a–c), the formation energy of $K_{Ta}+4O_N$ is close to that of K_{int} under the O-rich condition. For Li and Na, the formation energies of $M_{Ta}+4O_N$ are even lower than that of M_{int} under the O-rich condition, suggesting the possibilities of substitution-type doping for Li and Na. However, the Li, Na and K are expected to be doped at the interstitial site because of two reasons. Firstly, only the O-rich limit shows the predominance of substitutional doping, while more growth conditions show the predominance of interstitial doping. Secondly, even if under the O-rich limit, the formation energy difference between $Ma_{Ta}+4O_N$ and M_{int} is very small. Therefore, the Li, Na and K are expected to have more possibilities to be doped at the interstitial site. (b) In group IIA (Fig. 4d–g), the formation energy of $M_{Ta}+3O_N$ (M = Mg, Ca, Sr, Ba) is lower and larger than that of M_{int} under the O-rich and O-poor conditions, corresponding to the substitutional and interstitial doping, respectively. Furthermore, the chemical potential range of the substitutional doping is comparable to that of the interstitial doping. This is different from the situations of doping Li, Na and K that only the O-rich limit shows the predominance of substitutional doping. Therefore, the possibility of substitutional doping must be considered for Mg, Ca, Sr and Ba.

From the 24 elements, we screened out 6 elements (Li, Na, K, Cu, Ag, Au) which are preferentially to be doped at the interstitial site in Ta_3N_5. The left 18 elements (Mg, Ca, Sr, Ba, Al, Ga, In, Si, Ge, Sn, Zn, Cd, Sc, Y, La, Ti, Zr, Hf) are found to have more possibilities to substitute Ta and codope with O_N in Ta_3N_5. The following electronic structures calculations will be preformed based on these 18 elements.

3.2. Electronic structures

The density of states (DOS) of pure and O_N-doped Ta_3N_5 are shown in Fig. 5a and b, respectively. The DOS of $M_{Ta}+xO_N$ codoped Ta_3N_5 for 18 elements are shown in two columns. The DOS of $M_{Ta}+xO_N$ codoped Ta_3N_5 for elements in main groups (IIA, IIIA, IVA) and sub groups (IIB, IIIB, IVB) are shown in left column (Fig. 5c–l) and right column (Fig. 5o–v), respectively. On the top of right column, the DOS of pure and O_N-doped Ta_3N_5 are also shown in Fig. 5m and n, respectively, for the convenience of comparison. The band shift is calculated by aligning the electrostatic potentials between pure and elements doped Ta_3N_5 [59]. The electrostatic potentials of host elements far away from impurities are chosen as the reference energies. Furthermore, to help evaluate the band shift, we add two vertical red solid lines, which correspond to VBM and CBM, respectively, of the pure Ta_3N_5. In each case, the vertical dash line is the Fermi level. Fig. 5 reveals that:

(a) The major effects of O_N impurities on Ta_3N_5, which have been introduced in Fig. 1, are reduction of Ta atoms and cathodic shift of the CBM of Ta_3N_5. The reduction of Ta atoms can also be reflected by the location of Fermi level. Compared with the pure Ta_3N_5 (Fig. 5a), the Fermi level in O_N-doped Ta_3N_5 (Fig. 5b) cuts across conduction band, suggesting electron accumulation in the conduction band. Besides affecting the location of Fermi level, another important effect of elements doping is introducing in-gap states into the band gap of host materials [53]. In DOS of 18 $M_{Ta}+xO_N$ codoped Ta_3N_5, however, not only no in-gap states in the band gap, but also the Fermi level does not cut across any states. This means that the charge compensation between M_{Ta} and O_N can be successfully achieved for the 18 elements codoping models.

(b) For each of the 18 elements, the CBM of $M_{Ta}+xO_N$ codoped Ta_3N_5 shifts right and becomes higher than the water reduction potential (H^+/H_2) compared with that of the O_N-doped Ta_3N_5.

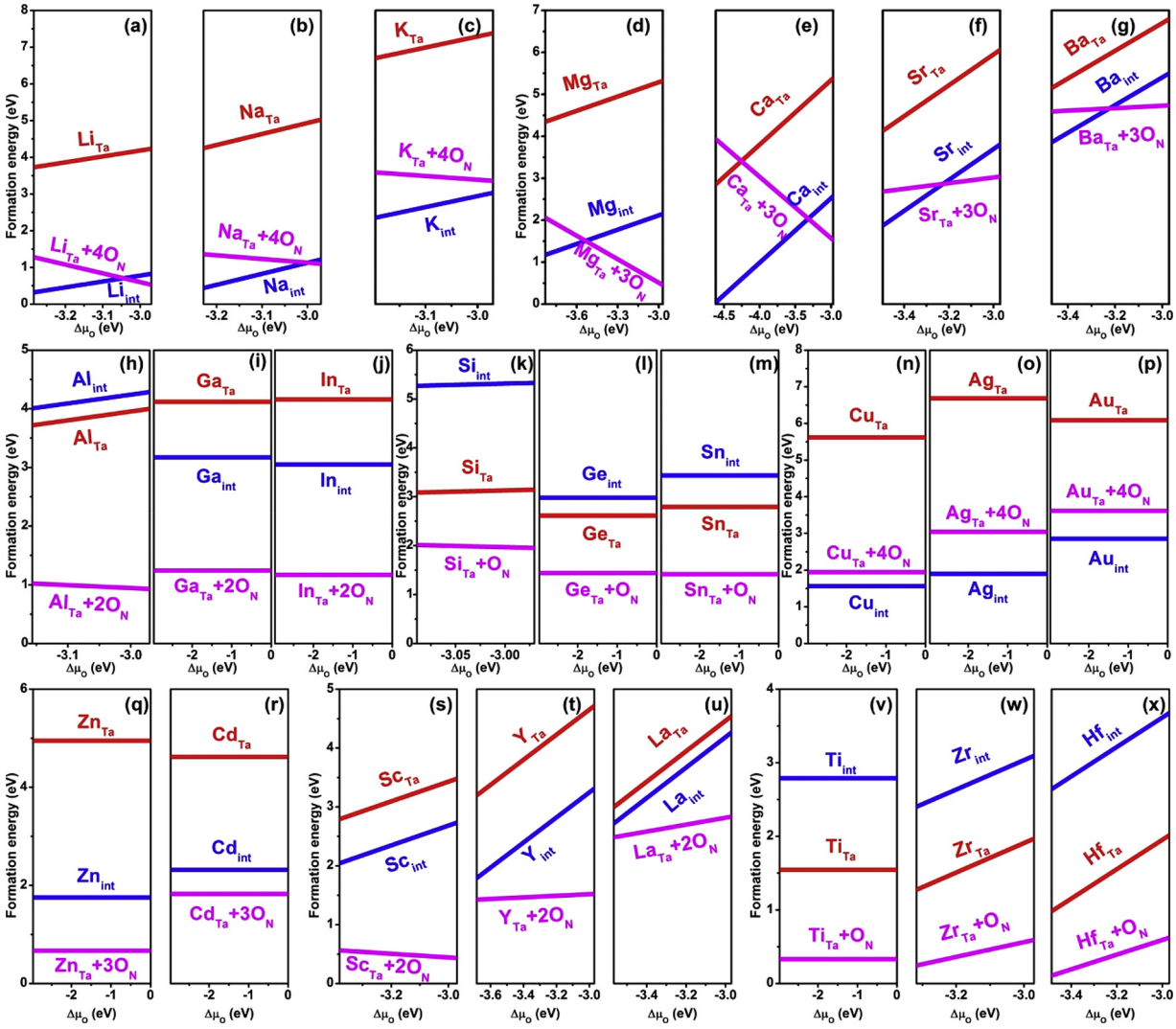

Fig. 4. Defect formation energies of doping 24 different $M_{Ta}+xO_N$ ($x = 1 \sim 4$) into Ta_3N_5 as a function of the chemical potential of O ($\Delta\mu_O$). The formation energies of M_{Ta} and M_{int} are also shown in each case. The 24 defect formation energy results are divided into 8 parts according to the groups of the 24 elements. In each part, defect formation energies use the same vertical axis range.

Furthermore, in the introduction section, we have mentioned that the CBM position of Ta_3N_5 is closely related to its onset potential in the PEC system. Therefore, our calculation results reveal that codoping each of the 18 elements with O_N is theoretically able to enhance the water reduction ability and lower the onset potential of Ta_3N_5. Further analysis of the CBM shift reveals an interesting result that, in some groups, the right shift of CBM of $M_{Ta}+xO_N$ codoped Ta_3N_5 gradually increases with the increase of atomic number. One possible explanation to this result is the gradually increased ionic radii of elements in each group. This result is especially obvious in group IIA because of the large variation of ionic radii from Mg (0.65 Å) to Ba (1.35 Å). When the variation of ionic radii is small, for example the Ti (0.68 Å), Zr (0.79 Å) and Hf (0.78 Å) in group IVB, this result is not obvious.

In this section, we find that codoping each of the 18 elements with O_N is able to shift the CBM of Ta_3N_5 to right. However, suitable CBM position is just one of the fundamental requirements for a photocatalytic semiconductor. When the electron and hole are generated on CBM and VBM after absorbing light energy, they will migrate to semiconductor surfaces and participate in the water reduction and oxidation reactions, respectively. Therefore, the mobility of electron and hole plays critical role in the water splitting reactions. Then, in the next section, we will calculate carrier effective masses to investigate effects of elements doping on the carrier mobility of Ta_3N_5.

3.3. Effective masses

The carrier effective mass (referenced to the electron rest mass m_0) is calculated from the equation [34]:

$$m = \frac{\hbar^2}{2\,|a|} \tag{3}$$

where $\hbar$ is the reduced Planck's constant, and a is the second derivative of the curve in conduction band (for electrons) and valence band (for holes). To obtain parameter a, the band structures will be calculated. Since the super-cell models are used in our study, the band structures calculated by super-cell may contain band folding effect [60,61]. Fig. 6a and b show band structures calculated by the primitive and conventional ($1 \times 1 \times 1$) cells, respectively, of the pure Ta_3N_5. Fig. 6a shows that Ta_3N_5 is an indirect gap semiconductor, with its VBM and CBM located at the Γ and Y points, respectively. Due to the Brillouin zone folding, however, both VBM and CBM in Fig. 6b locate at the Γ point. When we use the $3 \times 1 \times 1$ Ta_3N_5 super-cell, the band folding effect is still in the band structure (Fig. 6c). To correctly calculate carrier effective masses, we use the method proposed by Popescu et al. [60] to unfold the band structure calculated by super-cell. Fig. 6d shows the band structure of pure Ta_3N_5 unfolded from the $3 \times 1 \times 1$ super-cell, matching well with that of the primitive cell of Ta_3N_5 shown in

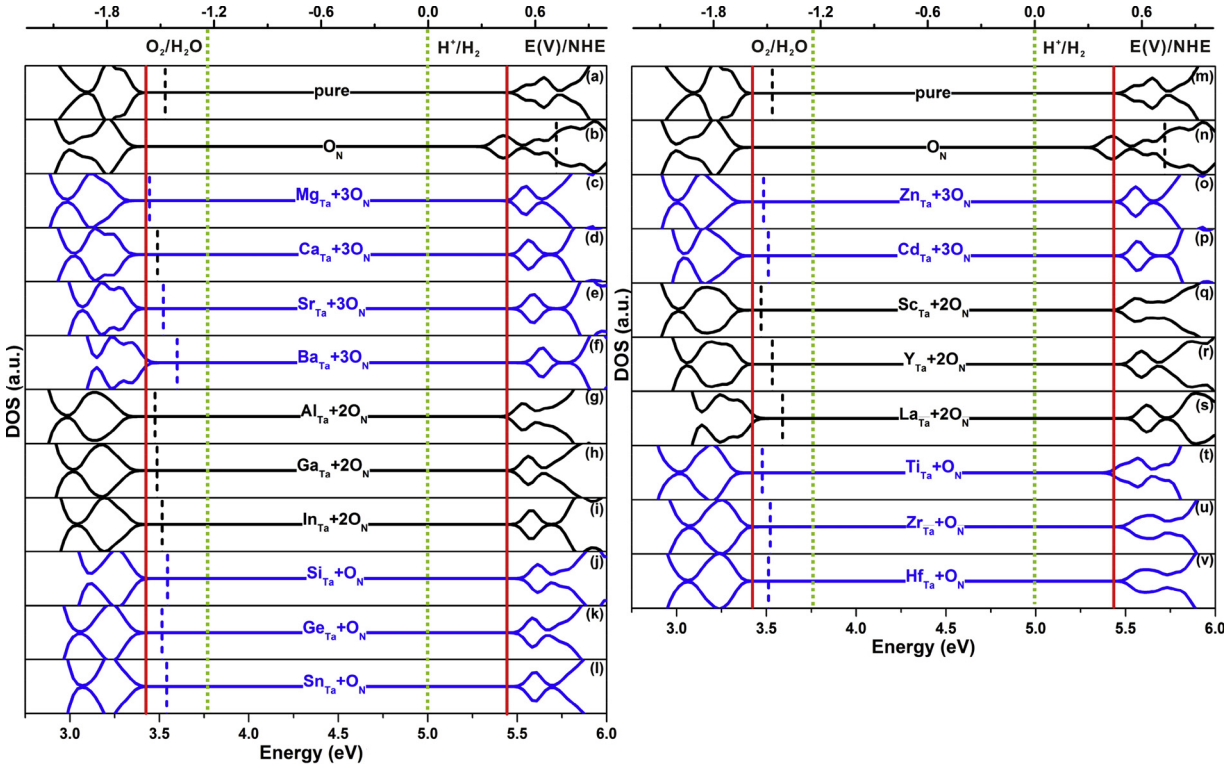

Fig. 5. The DOS of (a and m) pure, (b and n) O_N-doped and (c–l and o–v) $M_{Ta}+xO_N$ codoped Ta_3N_5. The vertical dash line in each case is the Fermi level. The horizontal axes of elements doped Ta_3N_5 are aligned with that of the pure Ta_3N_5 by the electrostatic potentials. Two vertical red solid lines, which correspond to the VBM and CBM of the pure Ta_3N_5, respectively, are added for the purpose of comparison. On the top of (a) and (m), the band edge positions of pure Ta_3N_5 with respect to normal hydrogen electrode (NHE) potential, which are obtained from experiment [10], are also shown. The two vertical green dot lines correspond to the water reduction (H^+/H_2) and oxidation (O_2/H_2O) potentials. (For interpretation of the references to colour in this figure legend, the reader is referred to the web version of this article.)

Fig. 6a. The Brillouin zones of primitive cell, conventional cell, and $3 \times 1 \times 1$ super-cell of Ta_3N_5 are put into SI-3 of the Supporting information.

Using the unfolded band structures, carrier effective masses of the pure and elements doped Ta_3N_5 are calculated and listed in Table 2. Note that, since the effective masses vary in different directions of the Brillouin zone, effective masses of electron and hole are calculated along some possible directions. As can be seen in Fig. 6a, since the CBM of Ta_3N_5 band structure locates at the high symmetry point Y, effective masses of the electron along Y→T and Y→Γ directions are calculated. For the hole, effective masses are calculated along Γ→Y and Γ→Z directions because the VBM of Ta_3N_5 locates at the Γ point.

Table 2 reveals that: (a) the carrier effective masses of electron along Y→T and Y→Γ directions of the O_N-doped Ta_3N_5 are lower and larger, respectively, than that of pure Ta_3N_5. Similarly, the effective masses of hole along Γ→Y and Γ→Z directions of the O_N-doped Ta_3N_5 are lower and larger, respectively, than that of pure Ta_3N_5. However, the effective masses of O_N-doped Ta_3N_5 are not changed a lot compared with that of the pure Ta_3N_5, suggesting that O_N doping does not significantly affect the carrier mobility of Ta_3N_5. (b) Except Ti, Zr and Hf in group IVB, codoping other elements with O_N substantially increase the carrier effective masses of Ta_3N_5. This means that doping elements in groups IIA, IIIA, IVA, IIB and IIB may lower the carrier mobility of Ta_3N_5. Note that, this does not mean that doping Ti, Zr or Hf is beneficial to the carrier mobility of Ta_3N_5. Actually, in $M_{Ta}+O_N$ (M = Ti, Zr, Hf) codoped Ta_3N_5, most of the carrier effective masses of elements codoped Ta_3N_5 are still larger than that of pure Ta_3N_5. However, the discrepancies in effective masses between pure and $M_{Ta}+O_N$ (M = Ti, Zr, Hf) codoped Ta_3N_5 are small. This means that codoping Ti, Zr or Hf with O_N may be not improve but at least not drastically destroy the carrier mobility of Ta_3N_5. In other words, doping Ti, Zr or Hf is able to keep the carrier mobility of Ta_3N_5. (c) What is worthy of mentioning is that, in each of groups IIA, IIIA, IVA, IIB and IIB, the effective masses along Y→Γ and Γ→Y directions increase with the increase of atomic number. This is similar with the situation of CBM shift in Fig. 5 and can also be ascribed to the gradually increased ionic radii in each group.

The effective masses, as well as the above defect formation energies and electronic structures, reveal that codoping Ti, Zr or Hf with O_N is relatively more effective to improve the photocatalytic and PEC activities of Ta_3N_5. However, we cannot completely exclude the possibilities of doping other 21 elements to improve the photocatalytic and PEC activities of Ta_3N_5. As mentioned above, the processes of photocatalytic and PEC water splitting are affected by various factors. Effective mass, formation energy and electronic structure are merely three fundamental factors. Furthermore, our calculations only provide a theoretical insight. The real performances of doping different elements into Ta_3N_5 still need experimental verifications. In the next section, we will further discuss some experiments of elements doped Ta_3N_5.

3.4. Further discussion

To our knowledge, Ta_3N_5 doped with different elements have been experimentally investigated in recent years [37–39,62–65]. Table 3 lists some representative PEC experiments of doping Ta_3N_5 with elements such as Ba [37], Sc [39], Mg [38], Zr [38], and Na [64,65]. We use the onset potential change and photocurrent change to express the effects of elements doping on PEC activities of Ta_3N_5. The onset potential change is the difference between onset potential of elements doped Ta_3N_5 and that of the undoped Ta_3N_5. Therefore, the negative onset potential change means the cathodic shift of onset potential. The photocurrent change is shown in percentage which is the result of photocurrent of element doped Ta_3N_5 divided by that of the undoped Ta_3N_5.

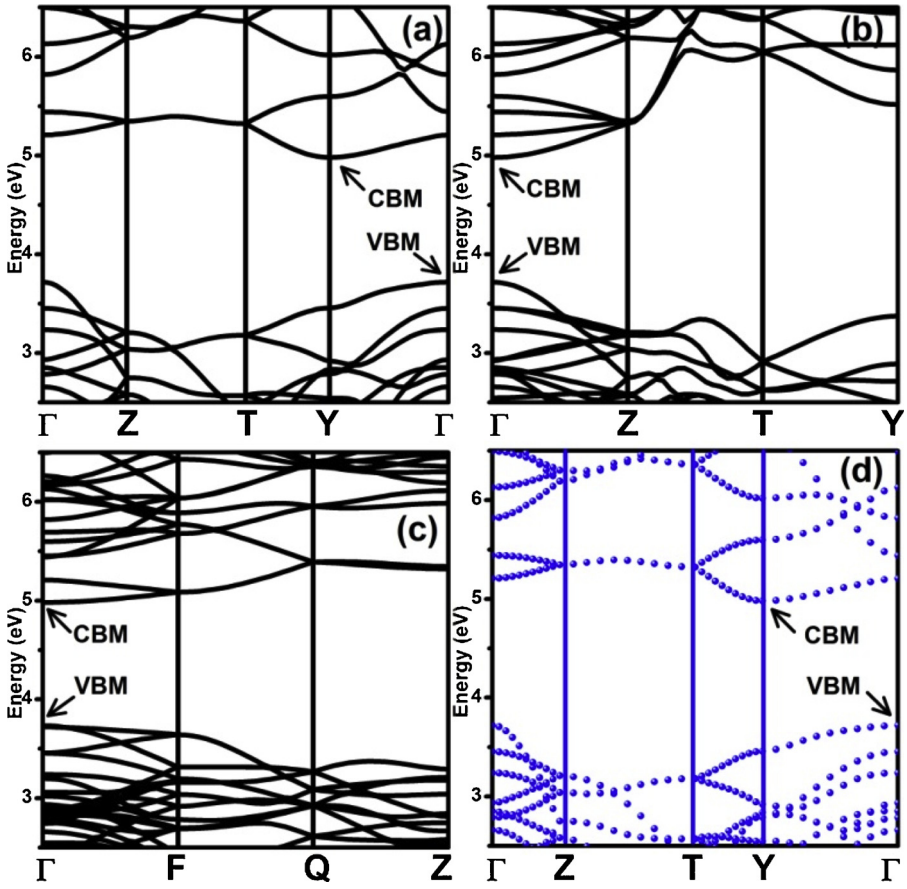

Fig. 6. Band structures of the (a) primitive cell, (b) conventional (1 × 1 × 1) cell and (c) 3 × 1 × 1 super-cell of the pure Ta_3N_5. (d) is the band structure of pure Ta_3N_5 unfolded from the 3 × 1 × 1 super-cell.

Table 2
Effective masses of electron and hole (relative to the electron rest mass) in the pure and elements doped Ta_3N_5 along different directions in the Brillouin zone of the pure Ta_3N_5.

Group of dopant	Doping model	electron		hole	
		Y→T	Y→Γ	Γ→Y	Γ→Z
/	pure	1.95	7.22	2.47	0.68
	O_N	1.82	7.71	2.37	0.88
IIA	$Mg_{Ta}+3O_N$	2.28	14.88	2.77	1.07
	$Ca_{Ta}+3O_N$	2.23	15.67	3.18	1.05
	$Sr_{Ta}+3O_N$	2.20	17.17	3.76	1.05
	$Ba_{Ta}+3O_N$	2.38	18.46	4.06	1.07
IIIA	$Al_{Ta}+2O_N$	2.18	10.27	2.56	1.12
	$Ga_{Ta}+2O_N$	2.26	11.99	2.79	1.09
	$In_{Ta}+2O_N$	2.28	15.34	2.86	1.10
IVA	$Si_{Ta}+O_N$	2.30	11.53	2.35	1.21
	$Ge_{Ta}+O_N$	2.20	13.96	2.35	1.19
	$Sn_{Ta}+O_N$	2.15	16.12	2.52	1.01
IIB	$Zn_{Ta}+3O_N$	2.32	17.76	3.08	1.06
	$Cd_{Ta}+3O_N$	2.31	24.83	3.46	1.07
IIIB	$Sc_{Ta}+2O_N$	2.07	8.11	2.46	1.07
	$Y_{Ta}+2O_N$	2.13	9.33	2.84	1.04
	$La_{Ta}+2O_N$	2.13	10.23	3.50	1.03
IVB	$Ti_{Ta}+O_N$	1.97	7.62	2.00	0.98
	$Zr_{Ta}+O_N$	1.94	7.67	2.78	0.82
	$Hf_{Ta}+O_N$	1.95	7.82	2.59	0.82

Table 3
The experimental onset potential change (in eV) and photocurrent change (in percentage) when some elements are doped into Ta_3N_5.

Dopants	Onset potential change	Photocurrent change
Ba [37]	−0.05	~125%
Sc [39]	−0.1	132%
Mg [38]	−0.1	~300%
Zr [38]	−0.25	~150%
Na [64,65]	Not reported	> 500%

Then, a larger percentage suggests the greater improvement of photocurrent.

Table 3 reveals that, the dopants Ba, Sc, Mg and Zr are all able to cathodically shift the onset potential of Ta_3N_5, agrees well with our calculated electronic structures. This also means that the charge compensation doping is indeed an effective method to lower the onset potential of Ta_3N_5. The different PEC performances of these five elements doped Ta_3N_5 can be understood by our calculated defect formation energies. The Zr-doped Ta_3N_5 shows a larger cathodic shift of onset potential than other four elements doped Ta_3N_5, which may be ascribed to the easily substitution of Zr for Ta. Compared with Ba, Sc and Zr, the Mg dopant induces about 300% improvement of photocurrent, which may be ascribed to the partially interstitial doping of Mg in Ta_3N_5. The dopant Na, which is preferentially doped at the interstitial site and acts as an electron donor, even induces a 500% improvement of photocurrent.

Experiments in Table 3 are all single element doped Ta_3N_5. The single element doping is difficult to lower onset potential and improve photocurrent of Ta_3N_5 simultaneously. Recent experiment of the Mg-Zr

codoped Ta_3N_5 photoanode achieved decreased onset potential and increased photocurrent simultaneously [38]. Theoretical calculations revealed that the enhanced PEC activities of Mg-Zr codoped Ta_3N_5 came from the different thermodynamic properties of Mg and Zr in Ta_3N_5 [57]. The Zr dopant preferentially substituted Ta and compensated for O_N, resulting in the cathodic shift of onset potential. The Mg dopant was partially doped at the interstitial site and acted as a delocalized electron donor, contributing to the enhanced photocurrent. In this study, we find that Ti, Zr and Hf are potentially substitutional candidates while Li, Na, K, Cu, Ag and Au are interstitial candidates in Ta_3N_5. Then, the combinations of these substitutional and interstitial candidates may be also able to lower onset potential and improve photocurrent of Ta_3N_5 simultaneously. We hope that our calculation results provide some useful guidance for future investigations of the elements codoped Ta_3N_5.

What is worthy of mentioning is that, besides elements doping, surface modification is another effective method to improve photocatalytic and PEC activities of semiconductors. In Table 3, the onset potential change of -0.1 V for Sc-doped Ta_3N_5 is the difference between Sc-doped and undoped Ta_3N_5 without surface modifications. When the $Co(OH)_x$ is deposited onto the surfaces of Sc-doped Ta_3N_5, the onset potential of Sc-doped Ta_3N_5 will further cathodically shift [39]. The same experimental phenomenon can also be found in the Mg-doped Ta_3N_5 after surface modifications [66]. Therefore, the combination of elements doping and surface modification is a potential method to further improve the photocatalytic and PEC activities of Ta_3N_5.

4. Conclusions

In summary, based on the DFT calculations, we investigated the effects of charge compensation doping on the photocatalytic and PEC activities of Ta_3N_5. We selected 24 possible elements to substitute Ta and compensate for the O_N impurity in Ta_3N_5. We firstly calculated defect formation energies and screened out 18 elements (Mg, Ca, Sr, Ba, Al, Ga, In, Si, Ge, Sn, Zn, Cd, Sc, Y, La, Ti, Zr, Hf) which have more thermodynamic possibilities to be codoped with O_N in Ta_3N_5. We secondly calculated electronic structures and found that all these 18 elements were theoretically able to enhance water reduction ability and lower onset potential of Ta_3N_5. Finally, we calculated effective masses and found that the dopants Ti, Zr and Hf were theoretically able to maintain the carrier mobility of Ta_3N_5. What should be emphasized is that, we cannot exclude the effectiveness of other 21 elements, as well as the elements we did not considered in this study, in improving the photocatalytic amd PEC activities of Ta_3N_5. We only hope that the further investigations of Ta_3N_5 will be enlightened from our theoretical study.

Acknowledgements

This work is supported by Fundamental Research Funds for the Central Universities (Grant No. 2016B14314, No. 2018B48414), National Natural Science Foundation of China (Grant No. 21503068, No. 51502339), and Key Research and development Project of Jiangsu Province (No. BE2016187).

Appendix A. Supplementary data

Supplementary material related to this article can be found, in the online version, at doi:https://doi.org/10.1016/j.apcatb.2018.11.076.

References

[1] M. Grätzel, Nature 414 (2001) 338–344.
[2] J. Seo, H. Nishiyama, T. Yamada, K. Domen, Angew. Chem. Int. Ed. 57 (2018) 8396–8415.
[3] Z.S. Li, W.J. Luo, M.L. Zhang, J.Y. Feng, Z.G. Zou, Energy Environ. Sci. 6 (2013) 347–370.
[4] C. Ding, J. Shi, Z. Wang, C. Li, ACS Catal. 7 (2017) 675–688.
[5] A. Fujishima, K. Honda, Nature 238 (1972) 37–38.
[6] W.J. Luo, Z.S. Yang, Z.S. Li, J.Y. Zhang, J.G. Liu, Z.Y. Zhao, Z.Q. Wang, S.C. Yan, T. Yu, Z.G. Zou, Energy Environ. Sci. 4 (2011) 4046–4051.
[7] A. Duret, M. Gratzel, J. Phys. Chem. B 109 (2005) 17184–17191.
[8] D. Chen, J. Ye, Adv. Funct. Mater. 18 (2008) 1922–1928.
[9] J.Y. Feng, W.J. Luo, T. Fang, H. Lv, Z.Q. Wang, J. Gao, W.M. Liu, T. Yu, Z.S. Li, Z.G. Zou, Adv. Funct. Mater. 24 (2014) 3535–3542.
[10] W.-J. Chun, A. Ishikawa, H. Fujisawa, T. Takata, J.N. Kondo, M. Hara, M. Kawai, Y. Matsumoto, K. Domen, J. Phys. Chem. B 107 (2003) 1798–1803.
[11] M.J. Liao, J.Y. Feng, W.J. Luo, Z.Q. Wang, J.Y. Zhang, Z.S. Li, T. Yu, Z.G. Zou, Adv. Funct. Mater. 22 (2012) 3066–3074.
[12] M. Hara, G. Hitoki, T. Takata, J.N. Kondo, H. Kobayashi, K. Domen, Catal. Today 78 (2003) 555–560.
[13] C. Zhou, J. Zhou, L. Lu, J. Wang, Z. Shi, B. Wang, L. Pei, S. Yan, Y. Zhentao, Z. Zou, Appl. Catal. B 237 (2018) 742–752.
[14] J. Cui, Y. Qi, B. Dong, L. Mu, Q. Ding, G. Liu, M. Jia, F. Zhang, C. Li, Appl. Catal. B 241 (2019) 1–7.
[15] E. Watanabe, H. Ushiyama, K. Yamashita, Catal. Sci. Technol. 5 (2015) 2769–2776.
[16] J.M. Morbec, I. Narkeviciute, T.F. Jaramillo, G. Galli, Phys. Rev. B 90 (2014) 155204.
[17] M. Harb, P. Sautet, E. Nurlaela, P. Raybaud, L. Cavallo, K. Domen, J.-M. Basset, K. Takanabe, Phys. Chem. Chem. Phys. 16 (2014) 20548–20560.
[18] T. Jing, Y. Dai, X.C. Ma, W. Wei, B.B. Huang, RSC Adv. 5 (2015) 59390–59397.
[19] X. Wang, H. Huang, G. Fan, Z. Li, Z. Zou, J. Phys. Chem. C 122 (2018) 489–494.
[20] L. Cui, M. Wang, Y.X. Wang, J. Phys. Soc. Jpn. 83 (2014) 114707.
[21] L. Wang, X. Zhou, N.T. Nguyen, I. Hwang, P. Schmuki, Adv. Mater. 28 (2016) 2432–2438.
[22] J.Y. Feng, D.P. Cao, Z.Q. Wang, W.J. Luo, J.J. Wang, Z.S. Li, Z.G. Zou, Chem. Eur. J. 20 (2014) 16384–16390.
[23] P. Zhang, J.J. Zhang, J.L. Gong, Chem. Soc. Rev. 43 (2014) 4395–4422.
[24] C. Zhen, R. Chen, L. Wang, G. Liu, H.-M. Cheng, J. Mater. Chem. A 4 (2016) 2783–2800.
[25] B.A. Pinaud, P.C.K. Vesborg, T.F. Jaramillo, J. Phys. Chem. C 116 (2012) 15918–15924.
[26] W.-P. Hsu, M. Mishra, W.-S. Liu, C.-Y. Su, T.-P. Perng, Appl. Catal. B 201 (2017) 511–517.
[27] S. Wang, Y. Guan, L. Lu, Z. Shi, S. Yan, Z. Zou, Appl. Catal. B 224 (2018) 10–16.
[28] G.J. Liu, S. Ye, P.L. Yan, F.Q. Xiong, P. Fu, Z.L. Wang, Z. Chen, J.Y. Shi, C. Li, Energy Environ. Sci. 9 (2016) 1327–1334.
[29] A.B. Murphy, P.R.F. Barnes, L.K. Randeniya, I.C. Plumb, I.E. Grey, M.D. Horne, J.A. Glasscock, Int. J. Hydrogen Energy 31 (2006) 1999–2017.
[30] S.J. Henderson, A.L. Hector, J. Solid State Chem. 179 (2006) 3518–3524.
[31] M. Ritala, P. Kalsi, D. Riihelä, K. Kukli, M. Leskelä, J. Jokinen, Chem. Mater. 11 (1999) 1712–1718.
[32] J.J. Wang, J.Y. Feng, L. Zhang, Z.S. Li, Z.G. Zou, Phys. Chem. Chem. Phys. 16 (2014) 15375–15380.
[33] J.J. Wang, A.B. Ma, Z.S. Li, J.H. Jiang, J.Y. Feng, Z.G. Zou, Phys. Chem. Chem. Phys. 17 (2015) 8166–8171.
[34] J.J. Wang, T. Fang, L. Zhang, J.Y. Feng, Z.S. Li, Z.G. Zou, J. Catal. 309 (2014) 291–299.
[35] A. Ishikawa, T. Takata, J.N. Kondo, M. Hara, H. Kobayashi, K. Domen, J. Am. Chem. Soc. 124 (2002) 13547–13553.
[36] B. Iandolo, B. Wickman, I. Zoric, A. Hellman, J. Mater. Chem. A 3 (2015) 16896–16912.
[37] Y.B. Li, L. Zhang, A. Torres-Pardo, J.M. Gonzalez-Calbet, Y.H. Ma, P. Oleynikov, O. Terasaki, S. Asahina, M. Shima, D. Cha, L. Zhao, K. Takanabe, J. Kubota, K. Domen, Nat. Commun. 4 (2013) 2566.
[38] J. Seo, T. Takata, M. Nakabayashi, T. Hisatomi, N. Shibata, T. Minegishi, K. Domen, J. Am. Chem. Soc. 137 (2015) 12780–12783.
[39] L. Pei, B. Lv, S. Wang, Z. Yu, S. Yan, R. Abe, Z. Zou, ACS Appl. Energy Mater. 1 (2018) 4150–4157.
[40] J. Li, Z. Zhang, W. Cui, H. Wang, W. Cen, G. Johnson, G. Jiang, S. Zhang, F. Dong, ACS Catal. 8 (2018) 8376–8385.
[41] J. Li, Xa. Dong, Y. Sun, G. Jiang, Y. Chu, S.C. Lee, F. Dong, Appl. Catal. B 239 (2018) 187–195.
[42] J. Li, W. Cui, Y. Sun, Y. Chu, W. Cen, F. Dong, J. Mater. Chem. A 5 (2017) 9358–9364.
[43] X. Lv, W. Wei, Q. Sun, F. Li, B. Huang, Y. Dai, Appl. Catal. B 217 (2017) 275–284.
[44] P. Zhao, Y. Ma, X. Lv, M. Li, B. Huang, Y. Dai, Nano Energy 51 (2018) 533–538.
[45] G. Kresse, J. Furthmüller, Comput. Mater. Sci. 6 (1996) 15–50.
[46] G. Kresse, J. Hafner, Phys. Rev. B 47 (1993) 558.
[47] P.E. Blöchl, Phys. Rev. B 50 (1994) 17953.
[48] J.P. Perdew, J. Chevary, S. Vosko, K.A. Jackson, M.R. Pederson, D. Singh, C. Fiolhais, Phys. Rev. B 46 (1992) 6671.
[49] J.P. Perdew, K. Burke, M. Ernzerhof, Phys. Rev. Lett. 77 (1996) 3865–3868.
[50] K. Momma, F. Izumi, J. Appl. Crystallogr. 44 (2011) 1272–1276.
[51] N.E. Brese, M. O'Keeffe, P. Rauch, F.J. DiSalvo, Acta Crystallogr. Sect. C: Cryst. Struct. Commun. 47 (1991) 2291–2294.
[52] A. Janotti, J. Varley, P. Rinke, N. Umezawa, G. Kresse, C. Van de Walle, Phys. Rev. B 81 (2010) 085212.
[53] P. Reunchan, N. Umezawa, S. Ouyang, J. Ye, Phys. Chem. Chem. Phys. 14 (2012) 1876–1880.
[54] J. Heyd, G.E. Scuseria, M. Ernzerhof, J. Chem. Phys. 118 (2003) 8207–8215.
[55] A.V. Krukau, O.A. Vydrov, A.F. Izmaylov, G.E. Scuseria, J. Chem. Phys. 125 (2006)

224106.
[56] C.G. Van de Walle, J. Neugebauer, J. Appl. Phys. 95 (2004) 3851–3879.
[57] J.J. Wang, A.B. Ma, Z.S. Li, J.H. Jiang, J.Q. Chen, Z.G. Zou, J. Mater. Chem. A 5 (2017) 6966–6973.
[58] J.J. Wang, A.B. Ma, Z.S. Li, J.H. Jiang, J.Y. Feng, Z.G. Zou, RSC Adv. 4 (2014) 55615–55621.
[59] W.J. Yin, H.W. Tang, S.H. Wei, M.M. Al-Jassim, J. Turner, Y.F. Yan, Phys. Rev. B 82 (2010) 045106.
[60] V. Popescu, A. Zunger, Phys. Rev. B 85 (2012) 085201.
[61] W. Ku, T. Berlijn, C.-C. Lee, Phys. Rev. Lett. 104 (2010) 216401.
[62] Y. Wang, D. Zhu, X. Xu, ACS Appl. Mater. Interfaces 8 (2016) 35407–35418.
[63] Y.H. Xie, Y.W. Wang, Z.F. Chen, X.X. Xu, ChemSusChem 9 (2016) 1403–1412.
[64] Y. Kado, R. Hahn, C.-Y. Lee, P. Schmuki, Electrochem. Commun. 17 (2012) 67–70.
[65] Y. Kado, C.-Y. Lee, K. Lee, J. Müller, M. Moll, E. Spiecker, P. Schmuki, Chem. Commun. 48 (2012) 8685–8687.
[66] L. Pei, Z. Xu, Z. Shi, H. Zhu, S. Yan, Z. Zou, J. Mater. Chem. A 5 (2017) 20439–20447.